

## Review Article

# Silicon Nanowires with Mesopores: Fabrication and Optical Properties

Zhifeng Huang<sup>1,3\*</sup> and Junjun Liu<sup>1</sup>

<sup>1</sup>Department of Physics, Hong Kong Baptist University (HKBU), China

<sup>2</sup>Institute of Advanced Materials, Hong Kong Baptist University, China

<sup>3</sup>HKBU Institute of Research and Continuing Education, Virtual University Park Building, China

\*Corresponding author

Zhifeng Huang, Department of Physics, Hong Kong Baptist University (HKBU), Institute of Advanced Materials, Hong Kong Baptist University, HKBU Institute of Research and Continuing Education, Virtual University Park Building, HKBU, Kowloon Tong, Hong Kong SAR, PR China, Tel: 852-3411-5886; E-mail: zhuang@hkbu.edu.hk

Submitted: 24 March 2015

Accepted: 18 June 2015

Published: 22 June 2015

Copyright

© 2015 Huang et al.

OPEN ACCESS

## Keywords

- Mesoporous silicon nanowires
- Metal-assisted chemical etching
- Photoluminescence
- Antireflection coating

## Abstract

Silicon nanowires (SiNWs) are electrochemically porosified to generate mesopores in sizes of 2-50 nm, resulting in the creation of mesoporous silicon nanowires (mpSiNWs). The porosification imposes two characteristics on to SiNWs: an increase of surface areas in the porous profile and quantum confinement ascribed to the shrinkage of silicon skeletons. Since the first report on producing mpSiNWs in 2009, the emerging porous nanostructures are increasingly catching fundamental and technical interests, and diverse but limited applications have been explored in batteries, energy storage, photocatalysis, drug delivery and gas sensors. In this mini review, we will elaborate the porosification mechanism in metal-assisted chemical etching of Si wafers that has been dominantly employed to fabricate mpSiNWs, in terms of intrinsic properties of Si wafers (i.e. the doping level and dopant elements), ingredients of the etching solution, temperature and complementary porosification methods. Among various physical properties of mpSiNWs, photoluminescence (PL) has been intensively studied owing to the promising application of mpSiNWs in optoelectronics. PL of mpSiNWs sensitively varies with the intrinsic properties of parent Si wafers, temperature and porosification processes, and the origin is still ambiguous and under debate. It will be reviewed the current studies in PL, together with the antireflection that is highly desired in producing green energy. At the end, it will be envisaged the prospects of mpSiNWs for developing the integrated optoelectronic devices.

## ABBREVIATIONS

mpSiNWs: Mesoporous Silicon Nanowires; mpSi: Mesoporous Silicon Layers; MACE: Metal-Assisted Chemical Etching; 1-MACE: One-Step MACE; 2-MACE: Two-step MACE; NPs: Nanoparticles; SHE: Standard Hydrogen Electrode;  $n/p$ :-:  $n/p$ -lightly-doped (electrical resistivity  $\rho > 0.1 \Omega\text{cm}$ );  $n^+/p^+$ :  $n/p$ -medially-doped ( $0.005 < \rho < 0.1 \Omega\text{cm}$ );  $n^{++}/p^{++}$ :  $n/p$ -heavily-doped ( $\rho < 0.005 \Omega\text{cm}$ ); PL: Photoluminescence; QC: Quantum Confinement; RRCs: Radiative Recombination Centers; NRCs: Non-Radiative Recombination Centers

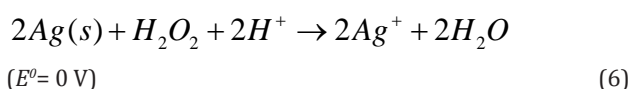
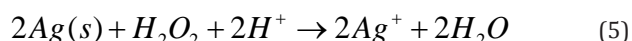
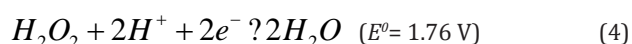
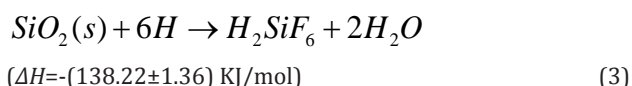
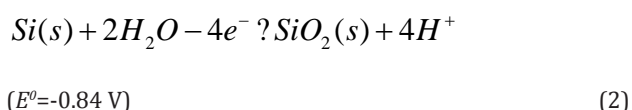
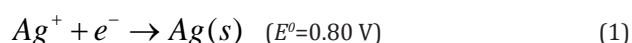
## INTRODUCTION

SiNWs appear to be solid long cylinders without pores. It has been reported in 2009 that SiNWs were electrochemically porosified to create mpSiNWs with pores in sizes of 2-50 nm (i.e. mesopores) [1,2]. mpSiNWs integrate the one-dimensional nanostructures with two porosification-induced effects, so as to increasingly catch fundamental and technical interests recently. The two porosification-caused effects include an increase in

surface area of the porous profile, and quantum confinement derived from the shrinkage in the residual Si skeletons. MACE has been predominantly employed to create mpSiNWs in a simple, low-cost way, and the fabrication mechanism will be fully reviewed. Compared to few reports on the properties of surface areas [1], electronic properties [1,2], surface hydrophobicity [3] and biodegradability [4], it has been intensively studied the optical properties of mpSiNWs, especially PL and antireflection. The porosification of SiNWs gives rise to various but limited applications in lithium ion batteries [5-7] energy storage [8], photocatalysis, [9] drug delivery, [10] and gas sensors [11]. These applications have been reviewed by Duan *et al.*, [12] and this mini review will mainly review the current studies in PL and antireflection of mpSiNWs.

## Fabrication of mpSiNWs

mpSiNWs are produced by MACE of Si wafers, an anisotropic, galvanic etching [13] involving a series of (electro)chemical reactions, givenby



The redox potential  $E$  is versus SHE.  $\Delta H$  is the reaction enthalpy, and the negative sign illustrates that a reaction generates heat. MACE is classified as 1-MACE and 2-MACE, which will be reviewed separately.

**MACE of medially and heavily doped Si wafers:** 1-MACE is generally operated in aqueous solution containing HF and  $\text{AgNO}_3$  [14], involving the nucleation of Ag NPs and scratching (or sinking) of the growing NPs into the bulky Si wafers [15].  $\text{Ag}^+$  ions in the vicinity of the wafer capture the electrons (eq. 1) that are donated by the anodic oxidation of Si (eq. 2), and then nucleate on the wafer surface. The Ag nucleation is thermodynamically ascribed to that Ag has electro negativity slightly higher than Si. HF dissolves the oxidized  $\text{SiO}_2$  (eq. 3) to create pits that trap the Ag nuclei. Ag NPs preferentially adhere to surface states, such as dangling bonds, structural defects (steps, kink sites, and dislocations) and sites around the do pants [16]. The oxidation of one Si atom generates four electrons (eq. 2), and the reduction of an  $\text{Ag}^+$  ion consumes only one electron (eq. 1). The excess electrons donated from the wafer migrate to and accumulate on the surfaces of Ag NPs, and electrostatically drive  $\text{Ag}^+$  ions diffuse towards the nuclei for reduction. Owing to abundant substances in the electrolyte and wafer, eq. 1-3 can subsequently and repeatedly take place. As a result, Ag NPs continuously scratch and sink into the wafer, and simultaneously grow into dendrites. The residual of the scratched wafer appears to be an array of SiNWs without pores, which retain the intrinsic electronic properties of the parent wafer [17]. The scratching of Ag NPs is prohibited along the lateral direction perpendicular to the substrate normal, since the etching rate determined by the curvature of a pore reaches the minimum along the lateral direction [18]. The sinking direction of growing NPs governs the surface crystalline orientation of as-generated SiNWs, and is comprehensively determined by the crystalline structure of parent wafers, etching temperature and duration, and electrolyte concentration [19,20].

Solid SiNWs are usually created by 1-MACE of lightly and medially doped wafers and the porosification of SiNWs will be triggered by increasing the doping level of wafers. For instance, 1-MACE of  $n^{++}\text{-Si}(100)$  creates mpSiNWs [21]. The heavy doping-induced porosification can be understood by a

thermodynamic model that describes charge transport across the silicon-electrolyte interface driven by potential energy (Figure 1a). Eq. 1 and 2 simply address the electron transport from Si to  $\text{Ag}^+$  ions, which is composed of the processes I-IV at the Si/electrolyte interface. Electrons at  $E_F$  of Si wafers migrate to the interface by overcoming a potential energy barrier  $\Delta\Phi$ , consisting of the excitation barrier ( $E_{CB}-E_F$ , the process I) and the band edge bending in SCL ( $E_{CB,S}-E_{CB}$ , the process II). Owing to the mismatch of  $E_{CB,S}$  with  $E_{Ag}^+$ , electrons are apt to relaxing to surface states ( $E_{SS}$ ) aligned with  $E_{Ag}^+$  (the process III) followed by the resonant migration to  $E_{Ag}^+$  (the process IV). The increase in the doping level not only up shifts  $E_F$  towards  $E_{CB}$  to reduce  $\Delta\Phi$ , but also makes the SCL thinner to promote electron tunneling through the SCL (Figure 1b), to facilitate the process I and II. Hence, a large amount of  $\text{Ag}^+$  ions nucleate on the surface and  $[\text{Ag}^+]$  (i.e. concentration of  $\text{Ag}^+$  ions) is significantly reduced in the electrolyte. Low  $[\text{Ag}^+]$  can support only a portion of Ag nuclei to grow and scratch the bulk Si. The rest non-grown Ag nuclei will undergo a random scratching in a short period of time to porosify SiNWs and the bulky wafer (Figure 1c). Since the scratching of growing Ag NPs is limited by the diffusion of  $\text{Ag}^+$  ions with low  $[\text{Ag}^+]$ , the random porosification tends to be faster than the NP scratching. Consequently, the electrochemical porosification tends to generate a hybrid structure composed of an array of mpSiNWs on mpSi (Figure 2a-d). On the contrary, the light and media doping increases  $\Delta\Phi$  to prevent  $\text{Ag}^+$  ions from severely consuming. High  $[\text{Ag}^+]$  substantially supports most Ag NPs grow and scratch the wafer to create SiNWs, and effectively suppresses the porosification (Figure 2e, f). This model can also account for the creation of mpSiNWs via 1-MACE of  $p^{++}\text{-Si}$  [1].

To promote the porosification in 1-MACE of  $n^{++}\text{-Si}$ , the process I and II are thermally excited via raising both the etching temperature from room temperature to 60 °C and  $[\text{HF}]$  from 2.4 mol/L to 5 mol/L [22]. The dissolution of  $\text{SiO}_2$  by HF is a heat-releasing reaction with a negative enthalpy (eq. 3), and the generated heat thermodynamically increases with  $[\text{HF}]$ . The thermal promotion of electron migration across the interfaces contributes to fabricating  $n^{++}\text{-mpSiNWs}$  (Figure 3a) with the porosity gradually decreasing from the tops to roots (Figure 3b-d), and there is a lack of mpSi underneath (Figure 3d). Compared to 1-MACE of  $n^{++}\text{-Si}$ , thermal excitation in 1-MACE of  $n^+\text{-Si}$  generates less non-grown NPs, and thus the porosification of non-grown Ag NPs occurs slower than the scratching of growing Ag NPs, accounting for the generation of the gradient porous structures without mpSi (Figure 4).

Both the doping level and electro negativity of do pants play a significant role in the electrochemical etching. For example, the do pants of  $n\text{-Si}$  include P with electro negativity of 2.19, as of 2.18 and Sb of 2.05, and function as the surface states ( $E_{SS}$ ). In 1-MACE of  $n^+\text{-Si}$ , the doping with Sb can generate SiNWs, [21] but the As-doping fails [2]. It is illuminated that the do pants are preferential to have small electro negativity for promoting the process IV. With respect to  $n^{++}\text{-Si}$ , a large amount of electrons accumulated in the vicinity of do pants overbalance the high electro negativity of As, so as to facilitate the process IV and create  $n^{++}\text{-mpSiNWs}$  via 1-MACE of As-doped  $n^{++}\text{-Si}$  [21]. In terms of  $n\text{-Si}$ , surface defects mainly serve as the surface states instead of the do pants that have relatively low concentration, to decouple the do pant electro

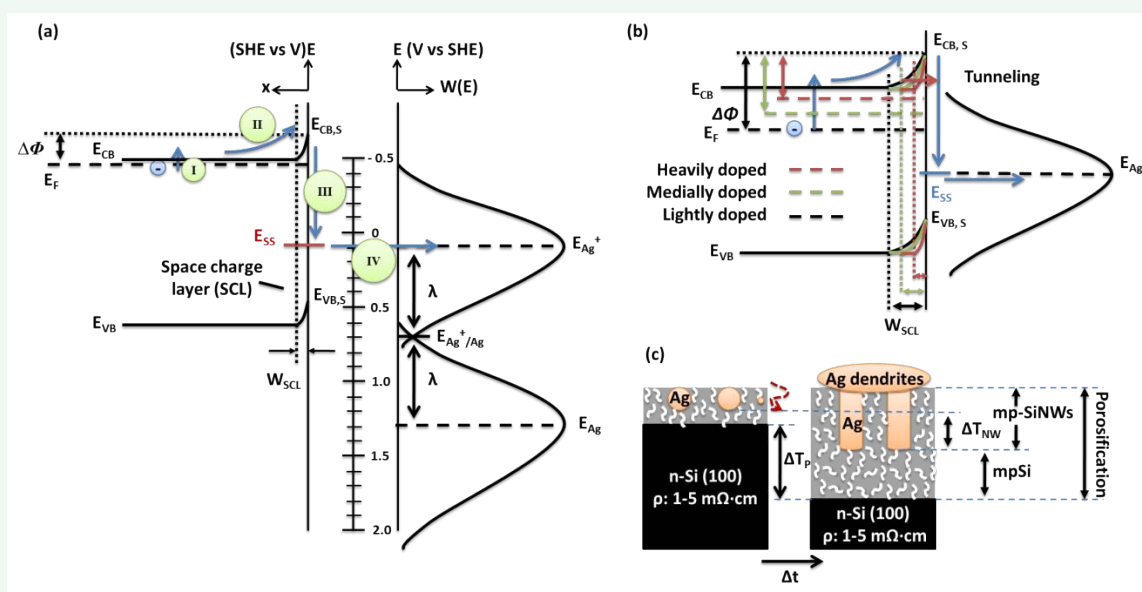


**Figure 1** (a) Quasi-quantitative energy diagram at the silicon-electrolyte interface, at the beginning of 1-MACE of  $n^{++}$ -Si(100). The energy is referred to standard hydrogen electrode (SHE) potential. Heavily doped n-Si has Fermi energy ( $E_F$ ), valence and conduction band in the bulk ( $E_{VB}$  and  $E_{CB}$ ) and at the interface ( $E_{VB,S}$  and  $E_{CB,S}$ ), and space charge layer (SCL) with a width  $W_{SCL}$ .  $\Delta\Phi$  is an energy barrier between  $E_F$  and  $E_{CB,S}$ .  $E_{Ag^+/Ag}$ ,  $E_{Ag^+}$  and  $E_{Ag}$  represent the potential energy of the redox pair,  $Ag^+$  and  $Ag$  in the electrolyte, respectively.  $\lambda$  is the reorientation energy. The light blue sphere represents an electron at  $E_F$  and the I-IV processes denote a subsequent series of electron migration from the bulk to interface. (b) Energy diagram with variation of doping levels in n-Si(100). (c) Schematic of the 1-MACE evolution. For clarity, it is shown only one non-grown Ag nucleus scratching the wafer in the mpSi, marked by a red dashed line. Within a period of time  $\Delta t$ , the evolution of the porosification and mp-SiNWs are denoted by  $\Delta T_p$  and  $\Delta T_{NW}$  respectively. (Adapted from Ref. [21]. Copyright 2011ACS Publications).

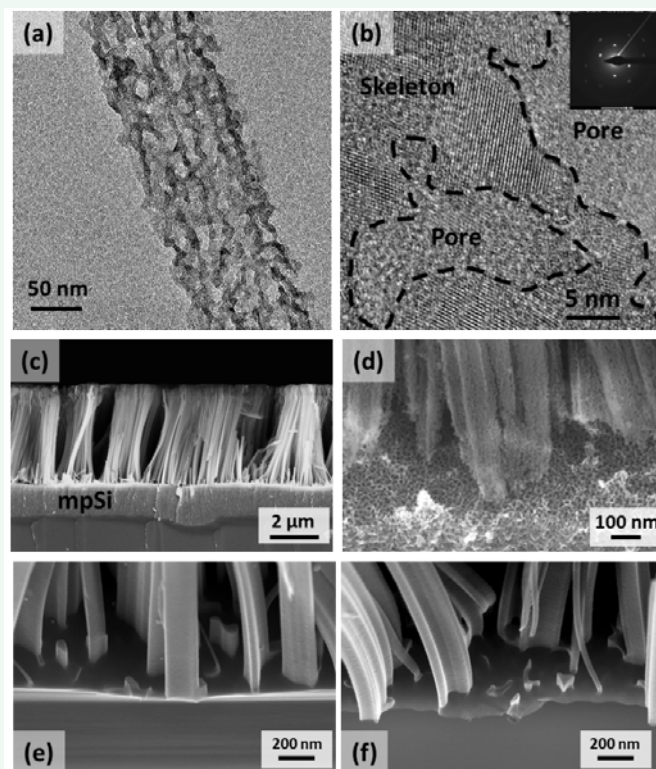


**Figure 2** 1-MACE of  $n^{++}$ -Si(100) generates mpSiNWs and a layer of porous Si (mpSi) underneath (a-d), and that of  $n$ -Si(100) (e) and  $n^{++}$ -Si(100) (f) creates SiNWs without mpSi. (a, b): TEM images; (c): SEM cross-sectional view; (d-f): SEM oblique views. (Adapted from Ref. [21]. Copyright 2011ACS Publications).

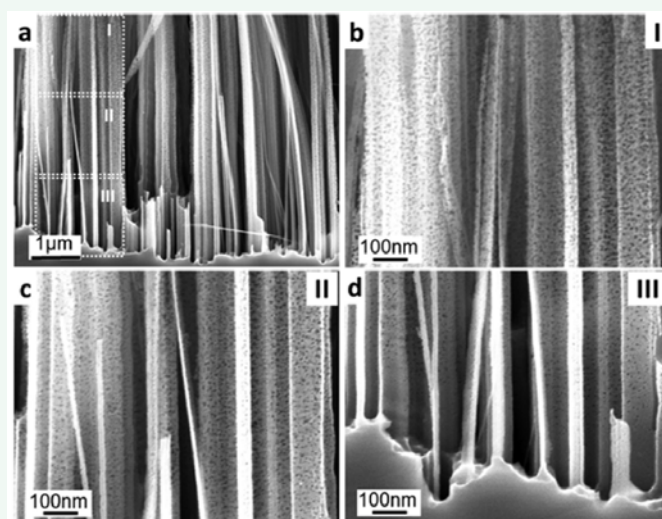


**Figure 3** (a) A SEM image of  $n^+$ -mpSiNWs. (b-d) High-magnification SEM images of the portion (I), (II) and (III) in (a). (Adapted from Ref. [22]. Copyright 2012ACS Publications).

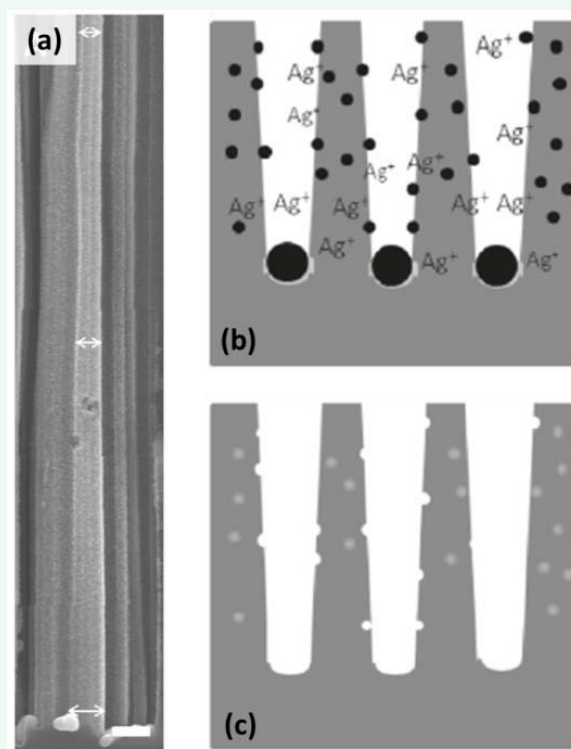


**Figure 4** (a) A SEM cross-sectional image of  $n^+$ -mpSiNWs having the trapezoid structure. (b,c) Schematic illustrations of the generation of trapezoid  $n^+$ -mpSiNWs via 2-MACE of  $n^+$ -Si. (Adapted from Ref. [29]. Copyright 2011ACS Publications).

negativity with the generation of SiNWs. Therefore, SiNWs can be fabricated by MACE of P-doped  $n^+$ -Si [17,21,23].

It is imperative to control the etching direction of growing Ag NPs for engineering surface crystalline orientation of mpSiNWs, [24] which plays a crucial role in catalysis, electronics and surface chemistry. The back-bond theory addresses that the etching along (100) need to cleave two Si-Si back bonds,

compared to three back bonds along (111) [16]. As a result, the etching is preferential along (100) over (111), which has been widely demonstrated in 1-MACE of Si(100), Si(111) and Si(110) [17,19,20,25,26]. However, Huang *et al.* found that under  $[HF]/[AgNO_3] \geq 50$ , 1-MACE of  $n^+$ -Si(111) has an intrinsic etching along [111] at room temperature, and the porosification in 1-MACE of  $n^+$ -Si(111) effectively disturbs the intrinsic etching [27]. The evolution of the porosification of non-grown NPs is faster than



the scratching of growing NPs, to weaken the back bonds in front of the scratching NPs and deviate the etching from (111). The etching preferentially switches to a direction with a small angle to (111), since the direction-switching barrier increases with the angle. The etching is preferential along  $\langle 211 \rangle$  at 10 °C, and  $\langle 311 \rangle$  at 20 °C. The intrinsic etching along (111) is reserved above 30 °C, due to the thermodynamic preference to the intrinsic etching. It is illuminated that the etching is governed by not only the back-bond etching, but also the crystalline structures of the as-etching wafers, concentration of etchants and etching temperature.

**MACE of medially and heavily doped Si wafers:** In 2-MACE, the nucleation of metal NPs and scratching of NPs are separately carried out [28]. The nucleation can be formed either by 1-MACE in a short period of time, or by the direct deposition of metal NPs in a random or periodic pattern. Then the etching is operated in aqueous HF solution containing strong oxidants (e.g.  $\text{H}_2\text{O}_2$ ) instead of metallic ions. Metal NPs adhere on the surface of Si wafers and function as catalysts. Since  $E^0_{\text{H}_2\text{O}_2/\text{H}_2\text{O}}$  is much more positive than  $E^0_{\text{SiO}_2/\text{Si}}$ ,  $\text{H}_2\text{O}_2$  diffusing to the vicinity of adhered NPs stimulates the oxidation of Si underneath the NPs (eq. 2), and the oxides are dissolved by HF (eq. 3). The released electrons enter into the NPs and migrate to the NP-electrolyte interfaces, followed by reducing  $\text{H}_2\text{O}_2$  (eq. 4). The subsequent repeated occurrence of (eq. 2-4) results in the scratching of adhered NPs to create SiNWs. If the catalysts NPs are made of Ag,  $E^0_{\text{H}_2\text{O}_2/\text{H}_2\text{O}}$  is also much more positive than  $E^0_{\text{Ag}^+/\text{Ag}}$ . Consequently,  $\text{H}_2\text{O}_2$  can oxidize Ag NPs into  $\text{Ag}^+$  ions (eq. 5). Note that in the 2<sup>nd</sup> step of 2-MACE, there is no  $\text{Ag}^+$  ion in the etching solution.  $\text{H}_2\text{O}_2$  with low concentration generates small amount of  $\text{Ag}^+$  ions in the vicinity of adhered Ag NPs, and the oxidized  $\text{Ag}^+$  ions most likely re-deposit onto the NPs. More  $\text{Ag}^+$  ions are generated with an increase of  $[\text{H}_2\text{O}_2]$ , and tend to diffuse away from the adhered NPs to the walls of as-generated SiNWs. Analogue to 1-MACE, the migrating  $\text{Ag}^+$  ions stimulate the electrochemical etching in the SiNWs' walls to roughen the surfaces of SiNWs at low  $[\text{H}_2\text{O}_2]$ , and to porosify SiNWs at high  $[\text{H}_2\text{O}_2]$  [29]. The porosity of mpSiNWs increases with  $[\text{H}_2\text{O}_2]$  [2]. The  $\text{H}_2\text{O}_2$ -induced dissolution of Ag NPs causes the catalyst NPs shrink during the etching (Figure 4b), to generate tapered mpSiNWs (Figure 4a,c) [29]. There is no mpSi underneath, since the scratching of shrunk Ag NPs is faster than the lateral porosification in the walls of SiNWs. The addition of surfactants (e.g. ethanol) in the 2<sup>nd</sup>-step etchant solution (HF and  $\text{H}_2\text{O}_2$ ) can effectively slow the scratching of Ag NPs, and thus generate a mpSi underneath mpSiNWs, even though the reason is ambiguous [4]. The diffusing  $\text{Ag}^+$  ions that are oxidized by  $\text{H}_2\text{O}_2$  preferentially nucleate on surface states nearby the do pants. The more do pants, the higher porosity SiNWs will have. Therefore, mpSiNWs are generally produced via 2-MACE of medially or heavily doped Si wafers. It should be emphasized that the porosification of SiNWs is attributed to the  $\text{H}_2\text{O}_2$ -induced oxidation of Ag NPs. To verify the role of  $\text{H}_2\text{O}_2$ ,  $\text{H}_2\text{O}_2$  was replaced with  $\text{Fe}(\text{NO}_3)_3$  [30]. Since  $E^0_{\text{Fe}^{3+}/\text{Fe}^{2+}}$  is slightly more negative than  $E^0_{\text{Ag}^+/\text{Ag}}$ ,  $\text{Fe}^{3+}$  ions thermodynamically fail to oxidize the adhered Ag NPs, so as to create SiNWs instead of mpSiNWs [31].

At  $[\text{H}_2\text{O}_2]$  of 0.5 mol/L, the porosity of mpSiNWs increases with [HF]. When [HF] is increased to 5.8 mol/L, the HF-induced dissolution of  $\text{SiO}_2$  is quick enough to remove the apexes of mpSiNWs, resulting in the formation of conical mpSiNWs [32].

When the nucleation is periodically patterned on Si wafers, 2-MACE can generate periodic arrays of mpSiNWs with controllable diameters and lengths. The template method includes nanosphere lithography, [33-35] anodic aluminum oxide mask method, [24] interference lithography, [36,37] superionic solid state stamping, [23] and block-copolymer mask method [38].

**Generation of mpSiNWs by MACE of lightly doped Si wafers:** Using both 1- and 2-MACE, mpSiNWs are generated from medially and heavily doped wafers. The light doping creates a high  $\Delta\Phi$  to suppress the electron transport process I and II, and to eliminate the porosification in SiNWs. To overcome the big  $\Delta\Phi$ , after the generation of n-SiNWs via 1-MACE of n-Si the wafer was further etched at a bias of 45 V and current density of 7 mA/cm<sup>2</sup> [3]. The electrochemical cell was composed of an anodic electrode of the n-Si wafer with n-SiNWs, and a cathodic electrode of a bare n-Si wafer. The electrolyte was an aqueous solution containing 4 mol/L HF and 3.2 mol/L  $\text{H}_2\text{O}_2$ . On the anodic electrode, the extremely high bias effectively drives the oxidation of Si (eq. 2) to cause the lateral porosification in SiNWs via eq. 3. The as-generated  $\text{H}^+$  ions (via eq. 2) electrically migrate to the cathode for reducing  $\text{H}_2\text{O}_2$  (eq. 4). The porosity of n-mpSiNWs increases with elongating the duration of the high-bias etching.

Another method of generating lightly doped mpSiNWs is 1-MACE of lightly doped Si wafers in the etching solution containing 4.6 mol/L HF, 0.02 mol/L  $\text{AgNO}_3$  and  $\text{H}_2\text{O}_2$  [39]. During 1-MACE, the scratching Ag NPs grow into a dendritic Ag layer to cover the wafer. The addition of  $\text{H}_2\text{O}_2$  generates a large amount of  $\text{Ag}^+$  ions by oxidizing Ag dendrites, resulting in the lateral porosification in the smooth walls of as-generated SiNWs. Low  $[\text{H}_2\text{O}_2]$  of 0.005 mol/L generates small amount of  $\text{Ag}^+$  ions, and only roughens SiNWs without porosification. mpSiNWs are created at  $[\text{H}_2\text{O}_2]$  increasing to 0.05 mol/L. The etching at >60 °C promotes the  $\text{H}_2\text{O}_2$ -induced oxidation of Ag dendrites and  $\text{Ag}^+$  ion diffusion, to facilitate the fabrication of mpSiNWs [40]. This method is adapted to n-Si and p-Si.

**Photoluminescence of mpSiNWs:** PL originates from the radiative recombination of excitons, which are optically generated by laser. The emission wavelength of PL is determined by the energy difference of two density of states between which the radiative recombination occurs [41]. The assignment of PL lies in identifying the nature of density of states, in which the recombining excitons stay. PL characteristics of mpSiNWs (i.e. the intensity, peak position  $\lambda_{\text{PL}}$  and decay time) are very sensitive to the doping level, [42] porosity and dangling bonds at the surfaces [43], Yang *et al.*, reported that in the ambient condition, p<sup>++</sup>-mpSiNWs have a broad, roughly symmetric PL peak centered at 680 nm (Figure 5a). They simply attributed the reddish PL to deep QC in the shrunk Si skeletons of p<sup>++</sup>-mpSiNWs, i.e. the direct radiative recombination across the Si band gap which is widened and transformed from indirect to direct due to the porosification-induced QC [1]. It is derived from QC that  $\lambda_{\text{PL}}$  of 680 nm requires to reduce the size of Si skeletons to 3-4 nm, which was verified by TEM of individual p<sup>++</sup>-mpSiNWs (Figure 5b). The broad peak is ascribed to wide distribution in the size of Si skeletons. The broad, symmetric reddish PL has been observed in n-mpSiNWs, [3] n<sup>+</sup>-mpSiNWs, [2,43] p<sup>+</sup>-mpSiNWs, [44] and n<sup>++</sup>-mpSiNWs [21].

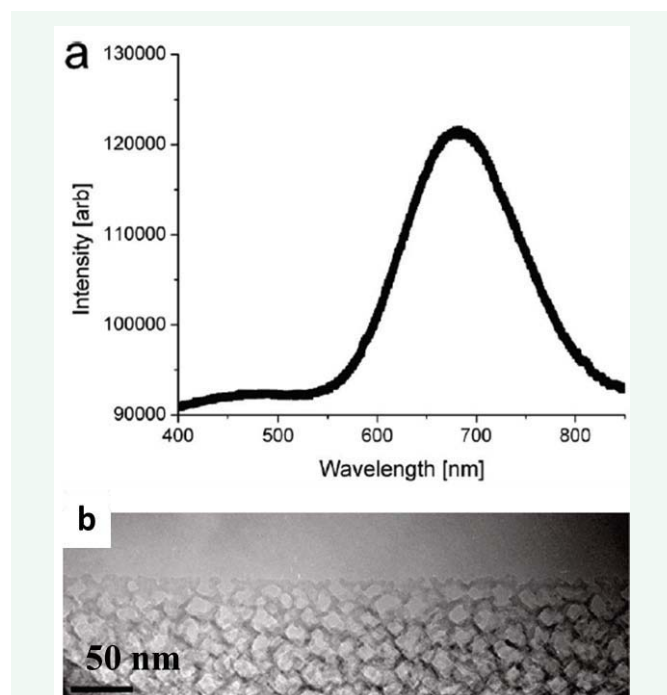


**Figure 5** (a) PL spectrum of  $p^+$ -mpSiNWs on  $p^+$ -Si. (b) A high-magnification TEM image of a  $p^+$ -mpSiNW. [Adapted from Ref. [1]. Copyright 2009ACS Publications].

However, it is under debate that the reddish PL originates from QC. First, QC predicts a blue shift of PL with increasing the porosity of mpSiNWs. Chiappini *et al.*, increased the porosity of  $p^+$ -mpSiNWs by raising  $[H_2O_2]$ . They found that low porosity have a broad PL spectrum centered at  $\sim 450$  nm, but high porosity causes a red shift of  $\lambda_{PL}$  to  $\sim 540$  nm [4]. Bai *et al.*, used 1-MACE to generate  $p^-$  and  $p^+$ -mpSiNWs. Compared to  $p^+$ -mpSiNWs with high porosity,  $p^-$ -mpSiNWs have porosity reducing from the sides to cores.  $p^-$ -mpSiNWs emit green PL, and  $p^+$ -mpSiNWs have reddish PL [39]. The red shift with porosity doesn't obey QC. Second, the oxidation of mpSiNWs shrinks Si skeletons and should make PL blue shift, according to QC. Focused laser with power larger than 55 mW was employed to oxidize  $n^+$ -mpSiNWs. The laser-induced oxidation effectively reduces the porosity (Figure 6a versus 6b). However, the reddish PL tends to slightly red shift from  $\sim 750$  nm to  $\sim 775$  nm (Figure 6c, as marked by the arrows) [45]. Third, electrochemical etching was used to fabricate  $n^-$ -mpSiNWs that have a broad reddish PL with  $\lambda_{PL}$  of 680 nm. It was from the TO (transverse optical)-phonon Raman mode located at  $520.7\text{ cm}^{-1}$  that the average size of silicon skeletons was evaluated as 6.6 nm [3]. QC substantially requires to have a characteristic size smaller than the Bohr radius of the free excitons of bulky Si ( $\sim 5$  nm), but the Si skeletons were evaluated larger than 5 nm [46]. Fourth, HF removes the oxide layers of  $n^+$ -mpSiNWs and significantly causes  $\lambda_{PL}$  red shift from  $\sim 700$  nm to  $\sim 800$  nm [47]. However, Si is intact in HF, so it is indicated by QC that the reddish PL not shift after the HF etching. The removal of oxides does affect

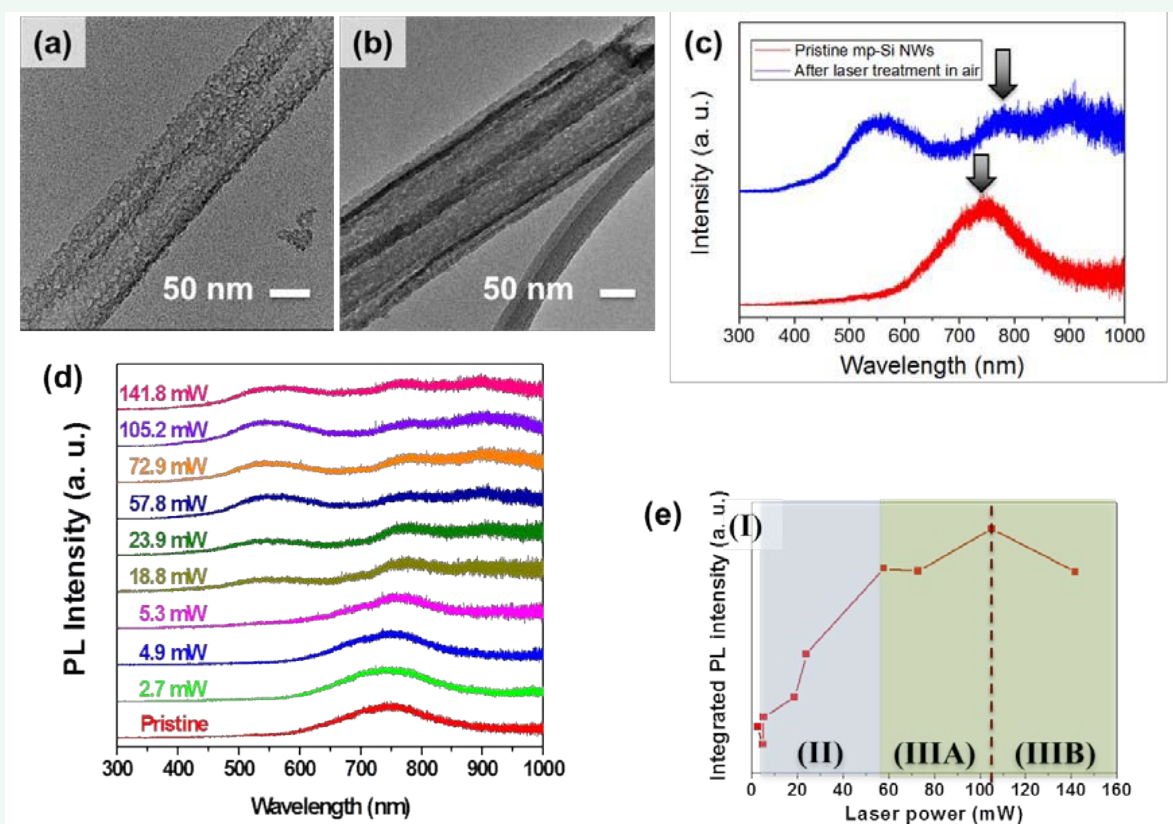


**Figure 6** TEM images: (a) pristine  $n^+$ -mpSiNWs, (b) laser-treated  $n^+$ -mpSiNWs. (c) PL spectrum of the pristine and laser-treated  $n^+$ -mpSiNWs. (d) PL spectrum of laser-treated  $n^+$ -mpSiNWs as function of laser power. (e) A plot of the integrated PL intensity (in the range of 400-600nm) versus laser power, divided into the region I, II, IIIA and IIIB. [Adapted from Ref. [45]. Copyright 2014 Nature Publishing Group].

the reddish PL, indicating that the reddish PL relate to surface states at the oxide/Si interfaces. The electrochemically-induced porosification of n-SiNWs significantly suppresses the vibrations of interfacial Si-O-Si, O-SiH<sub>x</sub> and SiH<sub>x</sub>, illustrating that the reddish PL should not be ascribed to hydrogenated amorphous Si, surface hydrides or polymer molecules on the surfaces [3]. It was proposed that surface states are the defects in the oxide layers [47]. XPS detects Si<sup>0</sup> (Si), Si<sup>+</sup> (Si<sub>2</sub>O), Si<sup>3+</sup> (Si<sub>2</sub>O<sub>3</sub>) and Si<sup>4+</sup> (SiO<sub>2</sub>) in n<sup>+</sup>-mpSiNWs. The surface defects could be Si<sup>+</sup> (Si<sub>2</sub>O) and Si<sup>3+</sup> (Si<sub>2</sub>O<sub>3</sub>) that are generated by dangling bonds and volumetric stress at the oxide/Si interfaces during the porosification [32].

Investigation in the dependence on temperature can shed light on the origin of the reddish PL of mpSiNWs covered with native oxides. p<sup>+</sup>-mpSiNWs emit reddish PL with  $\lambda_{PL}$  of ~650 nm at 300 K (Figure 7a), which red shifts from ~590 nm at 15 K to 650 nm at room temperature (Figure 7b). When the excitons migrate from RRCs to NRCs over an energy barrier, the excitons will undergo a non-radiative recombination to quench PL. The migration can be thermally promoted to overcome the RRCs-to-NRCs energy barrier, so the quenching is so-called thermal quenching. Thermal quenching accounts for that the PL intensity decreases gradually with temperature in the range of 12-160 K and 220-300 K (Figure 7c). There is a little increase in the range of 160-220 K, and a multi-level transition model was proposed to account for the negative thermal quenching [44]. In the ambient conditions, n<sup>+</sup>-mpSiNWs emit reddish PL centered at ~700 nm (Figure 7d), but have different dependence on temperature (Figure 7e) [21], Figure 7f shows that  $\lambda_{PL}$  tends to have small

fluctuation in the range of 16-220 K, followed by a red shift with temperature in the range of 220-290 K. The intensity gradually increases with temperature in the range of 16-160 K, ascribed to the thermo activated anti-trapping from surface defects in RRCs. Then the intensity diminishes with temperature in the range of 160-290 K, owing to thermal quenching. The reddish PL quenches quickly with temperature in the range of 160-220 K ascribed to high thermal quenching barrier of 150.6 meV, and reduces much more slowly in the range of 220-290 K attributed to small energy barrier of 31.2 meV. The different temperature dependence between p<sup>+</sup>- and n<sup>+</sup>-mpSiNWs may be ascribed to the diverse interfacial states, doping level and dopant elements.

The reddish PL of n<sup>+</sup>-mpSiNWs (Figure 8a) has  $\lambda_{PL}$  insensitive to temperature, excitation laser energy (Figure 8b) and laser power. But the PL intensity has a monotonous decrease with temperature in the range of 100-300 K (Figure 8c), increases with laser energy, and reaches the maximum at laser power of 0.35 mW [48]. When the oxides are removed by HF, the H-terminated n<sup>+</sup>-mpSiNWs emit a broad, asymmetric PL spectrum decomposed into two peaks: a reddish peak centered at ~730 nm and NIR peak (Figure 8d). The reddish and NIR PL both have the maximum intensity at 160 K (Figure 8e and 8f), but have different dependence of  $\lambda_{PL}$  on temperature and laser energy.  $\lambda_{PL}$  of the reddish PL is insensitive to temperature and laser energy, but the NIR PL blue shifts with temperature (Figure 8f) and laser energy. It was proposed that the triplet (T)-to-singlet (S) state transition dominates below 160 K. Owing to the exchange interaction of electrons and holes, the excitonic levels could split

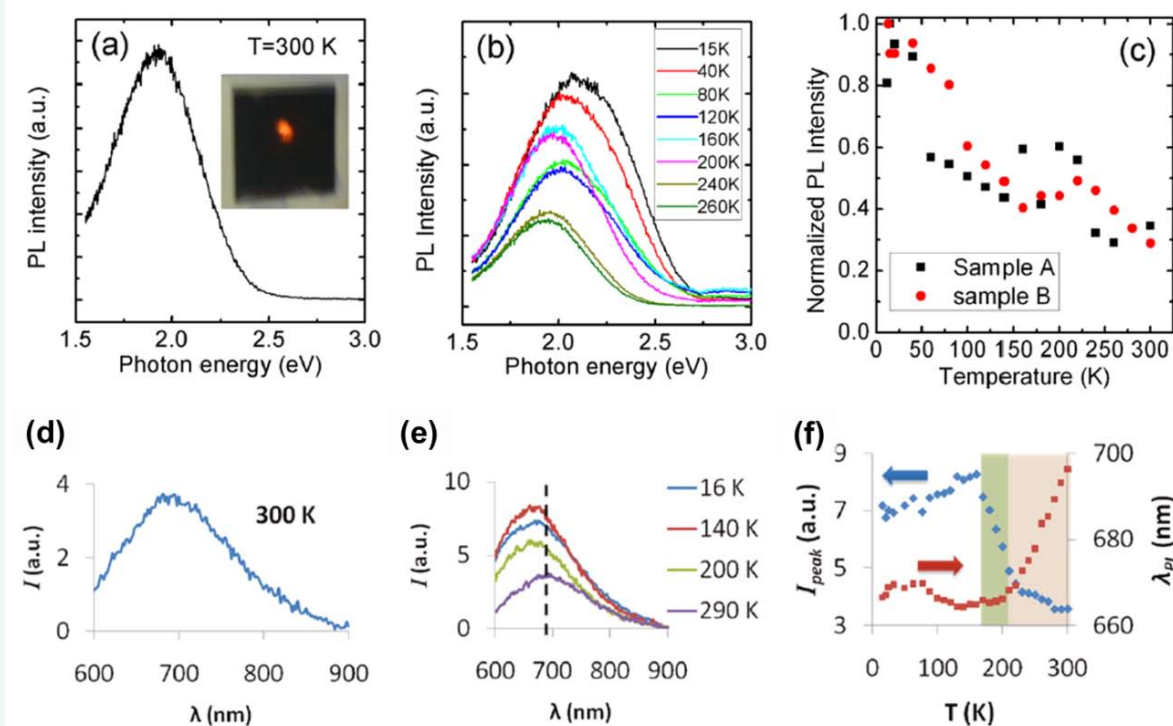


**Figure 7** (a) PL spectrum of p<sup>+</sup>-mpSiNWs at room temperature. Inset is the photograph of the p<sup>+</sup>-mpSiNW array under the illumination of He-Cd 325 nm laser. (b) Temperature-dependent PL spectra of p<sup>+</sup>-mpSiNWs. (c) Temperature-dependent PL peak intensity. (Adapted from Ref. [44]. Copyright 2011 AIP) (d) PL spectrum of n<sup>+</sup>-mpSiNWs at room temperature. (e) Temperature-dependent PL spectra of n<sup>+</sup>-mpSiNWs. (f) The plots of peak intensity and peak center versus temperature. (Adapted from Ref. [21]. Copyright 2011 ACS Publications).



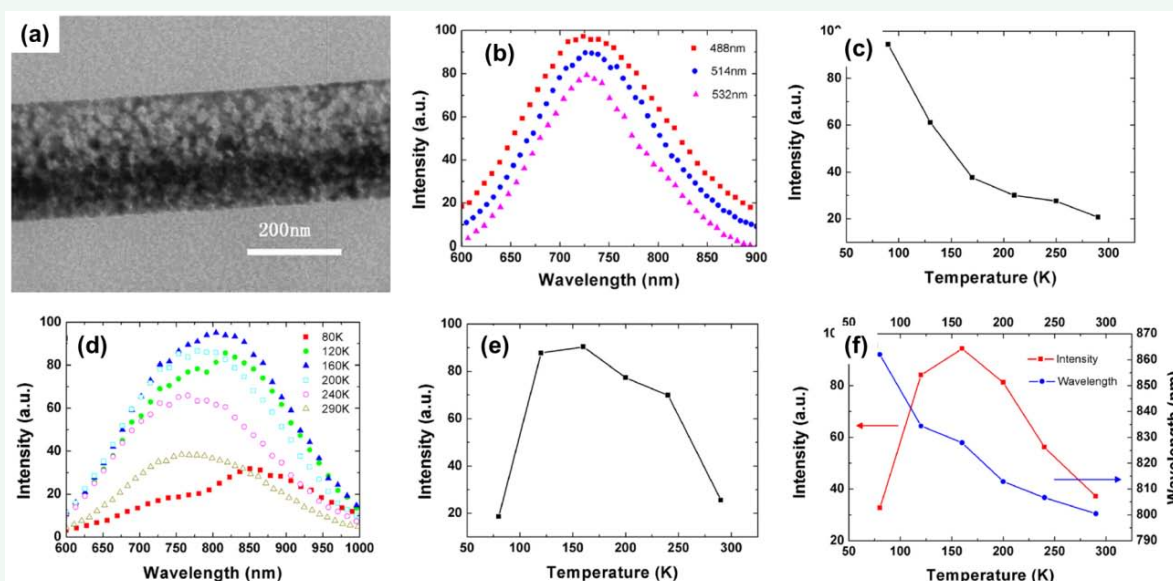


**Figure 8** (a) A TEM image of  $n^+$ -mpSiNW. (b) Excitation energy-dependent PL spectra of  $n^+$ -mpSiNW. (c) Temperature-dependent PL intensity. (d) Temperature-dependent PL spectra from 80 K to 290 K. (e) Temperature-dependent PL intensity for the red PL fixed at 730 nm. (f) Temperature-dependent PL intensity and peak wavelength of NIR PL. [Adapted from Ref. [48]. Copyright 2011 AIP].

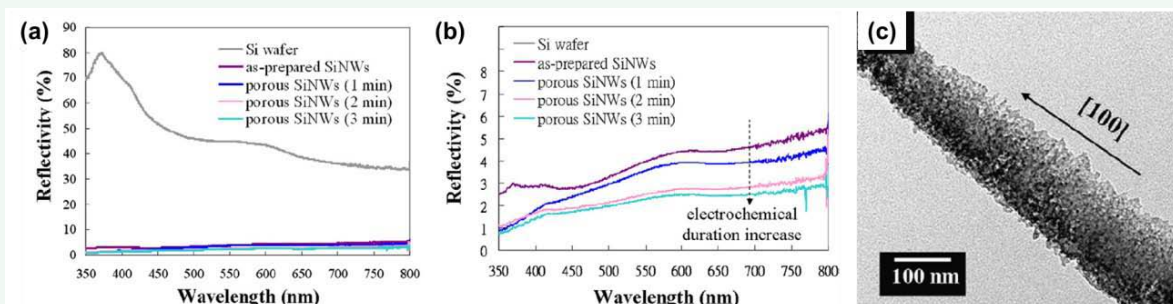


**Figure 9** (a) Reflective spectra of  $n$ -SiNWs and  $n$ -mpSiNWs.  $n$ -mpSiNWs were created by electrochemically porosifying  $n$ -SiNWs as function of porosification duration in the range of 1-3 min. (b) The zoom-in of (a) in the low reflective spectra. (c) A TEM image of a  $n$ -mpSiNW. [Adapted from Ref. [3]. Copyright 2012 Elsevier].

into a dipole-allowed upper singlet level and a dipole-forbidden lower triplet level. At low temperature, the excitons mainly occupy at the energetic favorable triplet state. The probability of T-to-S transition becomes higher with increasing temperature, leading to a raise of PL intensity. Above 160 K, thermal quenching tends to dominate over the T-to-S transition. The temperature-dependent tradeoff between the T-to-S transition and thermal quenching makes the reddish and NIR PL intensity reach the maximum at 160 K. The T-to-S transition happens in the H-terminated  $n^+$ -mpSiNWs. The transition-induced excitons can migrate from Si skeletons to interfacial states with smaller sizes nearby. The difference in the dependence of  $\lambda_{PL}$  on temperature and laser energy illustrates that the reddish and NIR PL originate from two different kinds of interfacial states. When  $n^+$ -mpSiNWs are covered with native oxides, the surface oxides prevent the T-to-S transition, resulting in the domination of thermal quenching in the range of 80-290 K (Figure 8c). In consistence, Lin *et al.*, reported that the PL spectrum of H-terminated  $n^+$ -mpSiNWs is decomposed into a reddish peak at  $\sim 750$  nm and

NIR peak at  $\sim 850$  nm [49]. The NIR PL enhances in intensity with the porosity faster than the reddish PL, leading to the red shift of the total broad PL spectrum with the porosity.

PL can be engineered by surface modification of mpSiNWs. Choi *et al.*, operated focused green laser to fast scan an array of  $n^+$ -mpSiNWs, and additionally generated a broad greenish-blue PL spectrum centered at  $\sim 550$  nm (Figure 6c) [45]. The threshold to excite the greenish-blue PL is the laser power of  $\sim 5$  mW, and the intensity increases with laser power in the range of 5-105 mW, followed by a quenching beyond 105 mW (Figure 6d-e). As characterized by Raman spectrum, in the region II (5-55 mW) the greenish-blue PL results from surface states generated by the laser-induced quick melting/re-solidification on the surfaces of  $n^+$ -mpSiNWs. Fast laser scanning causes surface oxidation in the region III ( $>55$  mW). In the region IIIA (55-105 mW), the greenish-blue PL is attributed to the oxide defects and oxygen holes in the oxide layers. The oxygen holes constructively couples with Si phonons to elongate the phonon lifetime, but the oxide



defects reduce the phonon lifetime by destructive interference. Beyond 105 mW (the region IIIB), the laser-induced oxide layers turn to be stoichiometric, resulting in a diminishment in the interfacial concentration of the oxygen holes and the dominant contribution of the oxide defects. The laser-induced up shift of density of states of the oxide defects causes a decrease in density of states in the greenish-blue band, accounting for the quenching beyond 105 mW. The greenish-blue PL can be enhanced by the post-laser annealing at 300 °C, in vacuum of  $10^{-2}$  Torr.

When p-mpSiNWs are conformally coated with 6-10 nm polycrystalline  $\text{SnO}_2$  by atomic layer deposition, PL appears to have a slight red shift from 510 to 530 nm [50]. By annealing the  $\text{SnO}_2$ -coated p-mpSiNWs in  $\text{N}_2/\text{H}_2$  at 600 °C,  $\text{SnO}_2$  is chemically decomposed into Sn, which diffuses into the Si skeletons to enhance PL. Zhang *et al.*, fabricated n<sup>+</sup>-mpSiNWs to emit a broad, symmetric PL spectrum centered at ~725 nm. n<sup>+</sup>-mpSiNWs were selenized at 700 °C in vacuum of  $4 \times 10^{-4}$  Pa [43,51]. FTIR shows the Si-Se bonds replace Si-H bonds on the surfaces, to passivate the dangling bonds and enhance PL stability during aging. XPS detects Si-Se at 54.9 eV and Si-Se-O at 56.3 eV, illustrating that sufficiently diffuses into n<sup>+</sup>-mpSiNWs. When exposed to a 532-nm laser, the selenized n<sup>+</sup>-mpSiNWs generate a broad PL spectrum decomposed into three peaks centered at 595, 645 and 715 nm. The peak centered at 595 nm and 645 nm are ascribed to the Si skeletons passivated by Si-Se-O and Si-Se, respectively. The third peak is retained from the pristine n<sup>+</sup>-mpSiNWs. The blue shift of the laser from 532 to 330 nm eliminates the reddish PL at 715 nm, and the two Se-related PL peaks blue shift from 595 to 510 nm and from 645 to 610 nm, respectively. The time-resolved PL spectrum was monitored to evaluate that PL stemming from Si-Se-O and Si-Se has an exciton lifetime of 2.68 and 0.49 ns, respectively. As comparison, the pristine n<sup>+</sup>-mpSiNWs emit the reddish PL at 715 nm with lifetime of 54  $\mu\text{s}$ . The significant reduce in the lifetime induced by the selenization accounts for the selenization-caused enhancement of PL. Furthermore, the selenization generates a broad NIR PL spectrum centered at ~1300 nm, probably attributed to the recombination of excitons in defect states.

## Antireflection of mpSiNWs

MACE generates an array of vertical mpSiNWs on a Si wafer, which functions as an antireflection coating to effectively reduce reflection loss of smooth wafers and magnify photovoltaic efficiency of Si-based solar cells [52]. The contribution of antireflection lies in two factors. First, incident light will be multiply reflected among close-packed vertical NWs to prevent light from escaping, i.e. optical trapping [53]. Second, an antireflection coating has an index of refraction to reduce the mismatch between the air and Si wafer. It is highly desirable for antireflection to have a tapered structure, in which the volume fraction of Si gradually reduces from the wafer surface to the air [54]. Compared to high reflectance of bare Si wafers in the range of 80%-36% in the UV-visible spectrum, n-SiNWs reduce reflectance to 2.5-5.5% mainly due to light trapping (Figure 9a) [3]. The electrochemical porosification of n-SiNWs can further reduce reflectance with increasing the porosity (Figure 9b), owing to the decrease in refraction index and increase in surface roughness (Figure 9c). However, To *et al.*, used an integrated sphere to measure scattering and transmittance, finding that an array of n<sup>++</sup>-mpSiNW strap less light and scatter more light than n<sup>++</sup>-SiNWs with the same thickness [53]. The porosification-enhanced light scattering may originate from the surface roughening induced by the porosification. Therefore, the enhanced antireflection with the porosity of n-mpSiNWs (Figure 9b) is more likely attributed to the tapered structures (Figure 9c). Recently, Charrier *et al.*, created n<sup>+</sup>-mpSiNWs that have not only the tapered profile (Figure 10a), but also the porosity gradually reducing from the top to root portions (Figure 10b) [47]. The gradient-porosity structures give rise to a graded decrease of refraction index from the Si wafer to the air, resulting in specular reflectance less than 0.1% in the UV-visible spectrum at an incident angle of 6° (Figure 10b). The elongation of tapered n<sup>+</sup>-mpSiNWs can further reduce reflection loss, owing to the enhancement of optical trapping (Figure 10c).

## Prospects

Optoelectronic devices substantially require an integration of

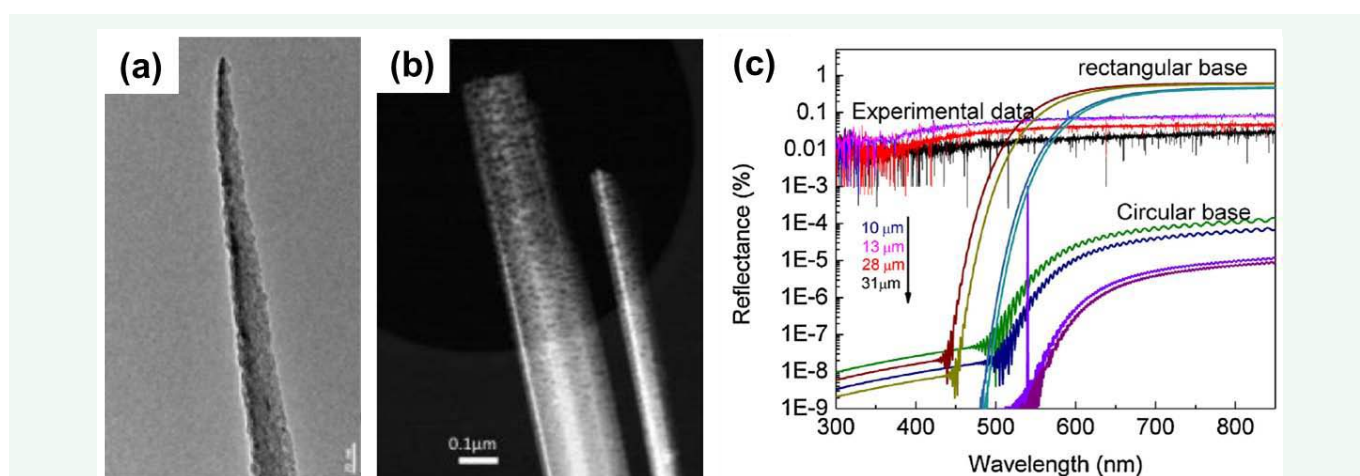


**Figure 10** TEM images: (a) a n<sup>+</sup>-mpSiNW with the cone shape, (b) two n<sup>+</sup>-mpSiNWs having graded porosity along their longitudinal axis. (c) Experimental and theoretical reflectance spectra of n<sup>+</sup>-mpSiNWs as function of the NW length. (Adapted from Ref. [47]. Copyright 2013 Elsevier).

tailorable electronic and optical properties of one-dimensional nanostructures, and there are some prospective outlooks for the investigation and development of mpSiNWs. First, It should be further studied charge transport in mpSiNWs, how much it deviates from parent Si wafers, the gate effect, and the dependence on the porosity. Second, surface modification plays an important role in enhancing anti-aging, passivating surface defects, tuning surface hydrophobicity, controlling exciton recombination, engineering charge transport, and improving chemical sensing. The grafting of SiNWs has been reported, including the silanization of  $\text{SiO}_x$ -covered SiNWs, hydrosilylation of H-terminated SiNWs, and two-step chlorination/alkylation of H-terminated SiNWs [55]. It should be explored the feasibility to impose these grafting approaches on to mpSiNWs. Third, the origin of PL is still ambiguous. Because PL is closely related to considerable amount of surface states/defects created by the porosification, the laser-induced doping of mpSiNWs in controlled environment (e.g. in  $\text{H}_2$ , Ar,  $\text{N}_2$ , organic solvents and polar solvents) could shed more light on the PL mechanism. Fourth, to make mpSiNWs adapted to a wide range of applications, it is highly desired the transfer of mpSiNWs onto a flexible, transparent substrate. Zheng *et al.*, generated a layer of cracks in an array of SiNWs by partially porosifying SiNWs [56]. The mechanical breakdown preferentially takes place at the crack layer, and thus a portion of SiNW arrays can be transferred to an adhesive. They also generated a sacrificial mpSi underneath the array of SiNWs by electro etching the parent Si wafers. The sacrificial mpSi significantly reduces the adhesion of SiNWs to the wafer, to facilitate the transfer to other substrates [57]. Analogously, 1-MACE directly creates a sacrificial mpSi beneath an array of  $n^+$ -mpSiNWs (Figure 2c-d), making it highly possible to transfer. For those without a sacrificial mpSi underneath, the porosification of parent Si wafers can be carried out by the electrochemical etching to create mpSi.

## ACKNOWLEDGEMENTS

We sincerely acknowledge the financial support of NSFC 21203010 (JJ) and ECS/RGC/HKBU 204412 (JJ).

## REFERENCES

- Hochbaum AI, Gargas D, Hwang YJ, Yang P. Single crystalline mesoporous silicon nanowires. *Nano Lett.* 2009; 9: 3550-3554.
- Qu Y, Liao L, Li Y, Zhang H, Huang Y, Duan X. Electrically conductive and optically active porous silicon nanowires. *Nano Lett.* 2009; 9: 4539-4543.
- Wang RC, Chao CY, Su WS. Electrochemically controlled fabrication of lightly doped porous Si nanowire arrays with excellent antireflective and self-cleaning properties. *Acta Materialia.* 2012; 60: 2097-2103.
- Chiappini C, Liu X, Fakhoury JR, Ferrari M. Biodegradable porous silicon barcode nanowires with defined geometry. *Adv Funct Mater.* 2010; 20: 2231-2239.
- Yoo JK, Kim J, Lee H, Choi J, Choi MJ, Sim DM, et al. Porous silicon nanowires for lithium rechargeable batteries. *Nanotechnology.* 2013; 24: 424008.
- Ge M, Rong J, Fang X, Zhou C. Porous doped silicon nanowires for lithium ion battery anode with long cycle life. *Nano Lett.* 2012; 12: 2318-2323.
- Jia HP, Gao PF, Yang J, Wang JL, Nuli YN, et al. Novel Three-Dimensional Mesoporous Silicon for High Power Lithium-Ion Battery Anode Material. *Adv Energy Mater.* 2011; 1: 1036-1039.
- Wang XL, Han WQ. Graphene enhances Li storage capacity of porous single-crystalline silicon nanowires. *ACS Appl Mater Interfaces.* 2010; 2: 3709-3713.
- Qu Y, Zhong X, Li Y, Liao L, Huang Y, Duan X. Photocatalytic Properties of Porous Silicon Nanowires. *J Mater Chem.* 2010; 20: 3590-3594.
- Xue M, Zhong X, Shaposhnik Z, Qu Y, Tamanoi F, Duan X, et al. pH-Operated mechanized porous silicon nanoparticles. *J Am Chem Soc.* 2011; 133: 8798-8801.
- Peng KQ, Wang X, Lee ST. Gas sensing properties of single crystalline porous silicon nanowires. *Appl Phys Lett.* 2009; 95: 243112.
- Qu Y, Zhou H, Duan X. Porous silicon nanowires. *Nanoscale.* 2011; 3: 4060-4068.
- Li X, Bohn PW. Metal-assisted chemical etching in  $\text{HF}/\text{H}_2\text{O}_2$  produces porous silicon. *Appl Phys Lett.* 2000; 77: 2572-2574.
- Peng KQ, Yan YJ, Gao SP, Zhu J. Synthesis of large-area silicon nanowire arrays via self-assembling nanoelectrochemistry. *Adv Mater.* 2002; 14: 1164-1167.
- Peng KQ, Yan YJ, Gao SP, Zhu J. Dendrite-assisted growth of silicon nanowires in electroless metal deposition. *Adv Funct Mater.* 2003; 13: 127-132.
- Morinaga H, Suyama M, Ohmi T. Mechanism of Metallic Particle Growth and Metal-Induced Pitting on Si Wafer Surface in Wet Chemical-Processing. *J Electrochem Soc.* 1994; 141: 2834-2841.
- Peng KQ, Lu AJ, Zhang RQ, Lee ST. Motility of Metal Nanoparticles in Silicon and Induced Anisotropic Silicon Etching. *Adv Funct Mater.* 2008; 18: 3026-3035.
- Zhang XG. Mechanism of pore formation on n-type silicon. *J Electrochem Soc.* 1991; 138: 3750-3756.
- Chen H, Wang H, Zhang XH, Lee CS, Lee ST. Wafer-scale synthesis of single-crystal zigzag silicon nanowire arrays with controlled turning angles. *Nano Lett.* 2010; 10: 864-868.
- Chen CY, Wu CS, Chou CJ, Yen TJ. Morphological Control of Single-Crystalline Silicon Nanowire Arrays near Room Temperature. *Adv Mater.* 2008; 20: 3811-3815.
- To WK, Tsang CH, Li HH, Huang Z. Fabrication of n-type mesoporous silicon nanowires by one-step etching. *Nano Lett.* 2011; 11: 5252-5258.
- Yuan GD, Mitdank R, Mogilatenko A, Fischer SF. Porous Nanostructures and Thermoelectric Power Measurement of Electro-Less Etched Black Silicon. *J Phys Chem C.* 2012; 116: 13767-13773.
- Chern W, Hsu K, Chun IS, de Azeredo BP, Ahmed N, Kim KH, et al. Nonlithographic Patterning and Metal-Assisted Chemical Etching for Manufacturing of Tunable Light-Emitting Silicon Nanowire Arrays. *Nano Lett.* 2010; 10: 1582-1588.
- Huang ZP, Shimizu T, Senz S, Zhang Z, Zhang XX, Lee W, et al. Ordered Arrays of Vertically Aligned [110] Silicon Nanowires by Suppressing the Crystallographically Preferred Etching Directions. *Nano Lett.* 2009; 9: 2519-2525.
- Fang H, Li X, Song S, Xu Y, Zhu J. Fabrication of slantingly-aligned silicon nanowire arrays for solar cell applications. *Nanotechnology.* 2008; 19: 255703.
- Zhang ML, Peng KQ, Fan X, Jie JS, Zhang RQ, Lee ST, et al. Preparation of large-area uniform silicon nanowires arrays through metal-assisted chemical etching. *J Phys Chem C.* 2008; 112: 4444-4450.
- Bai F, To WK, Huang ZF. Porosification-Induced Back-Bond Weakening

- in Chemical Etching of n-Si(111). *J Phys Chem C*. 2013; 117: 2203-2209.
28. Huang Z, Geyer N, Werner P, de Boor J, Gösele U. Metal-assisted chemical etching of silicon: a review. *Adv Mater*. 2011; 23: 285-308.
  29. Zhong X, Qu Y, Lin YC, Liao L, Duan X. Unveiling the formation pathway of single crystalline porous silicon nanowires. *ACS Appl Mater Interfaces*. 2011; 3: 261-270.
  30. Peng KQ, Wu Y, Fang H, Zhong XY, Xu Y, Zhu J. Uniform, axial-orientation alignment of one-dimensional single-crystal silicon nanostructure arrays. *Angew Chem-Int Edit*. 2005; 44: 2737-2742.
  31. Peng KQ, Hu JJ, Yan YJ, Wu Y, Fang H, Xu Y, et al. Fabrication of single-crystalline silicon nanowires by scratching a silicon surface with catalytic metal particles. *Adv Funct Mater*. 2006; 16: 387-394.
  32. Najar A, Slimane AB, Hedhili MN, Anjum D, Sougrat R, Ng TK, et al. Effect of hydrofluoric acid concentration on the evolution of photoluminescence characteristics in porous silicon nanowires prepared by Ag-assisted electroless etching method. *J Appl Phys*. 2012; 112: 033502.
  33. Huang ZP, Fang H, Zhu J. Fabrication of silicon nanowire arrays with controlled diameter, length, and density. *Adv Mater*. 2007; 19: 744-748.
  34. Peng KQ, Zhang ML, Lu AJ, Wong NB, Zhang RQ, et al. Ordered silicon nanowire arrays via nanosphere lithography and metal-induced etching. *Appl Phys Lett*. 2007; 90: 163123.
  35. Mikhael B, Elise B, Xavier M, Sebastian S, Johann M, Laetitia P. New silicon architectures by gold-assisted chemical etching. *ACS Appl Mater Interfaces*. 2011; 3: 3866-3873.
  36. Choi WK, Liew TH, Dawood MK, Smith HI, Thompson CV, Hong MH. Synthesis of silicon nanowires and nanofin arrays using interference lithography and catalytic etching. *Nano Lett*. 2008; 8: 3799-3802.
  37. Chang SW, Chuang VP, Boles ST, Thompson CV. Metal-Catalyzed Etching of Vertically Aligned Polysilicon and Amorphous Silicon Nanowire Arrays by Etching Direction Confinement. *Adv Funct Mater*. 2010; 20: 4364-4370.
  38. Chang SW, Chuang VP, Boles ST, Ross CA, Thompson CV. Densely Packed Arrays of Ultra-High-Aspect-Ratio Silicon Nanowires Fabricated using Block-Copolymer Lithography and Metal-Assisted Etching. *Adv Funct Mater*. 2009; 19: 2495-2500.
  39. Bai F, Li MC, Song DD, Yu H, Jiang B, Li YF. One-step synthesis of lightly doped porous silicon nanowires in HF/AgNO<sub>3</sub>/H<sub>2</sub>O<sub>2</sub> solution at room temperature. *J Solid State Chem*. 2012; 196: 596-600.
  40. Chen HH, Zou RJ, Chen HH, Wang N, Sun YG, Tian QW, et al. Lightly doped single crystalline porous Si nanowires with improved optical and electrical properties. *J Mater Chem*. 2011; 21: 801-805.
  41. Jing LQ, Qu YC, Wang BQ, Li SD, Jiang BJ, Yang LB, et al. Review of photoluminescence performance of nano-sized semiconductor materials and its relationships with photocatalytic activity. *Sol Energy Mater Sol Cells*. 2006; 90: 1773-1787.
  42. Lettieri S, Maddalena P, Di Francia G, Morvillo P. Influence of doping concentration on the photoluminescence of silicon nanocrystals. *Phys Status Solidi A-Appl Res*. 2003; 197: 399-402.
  43. Lin L, Sun X, Tao R, Feng J, Zhang Z. The synthesis and photoluminescence properties of selenium-treated porous silicon nanowire arrays. *Nanotechnology*. 2011; 22: 075203.
  44. He HP, Liu C, Sun LW, Ye ZZ. Temperature-dependent photoluminescence properties of porous silicon nanowire arrays. *Appl Phys Lett*. 2011; 99: 123106.
  45. Choi YR, Zheng M, Bai F, Liu J, Tok ES, Huang Z, Sow et al. Laser-induced greenish-blue photoluminescence of mesoporous silicon nanowires. *Sci Rep*. 2014; 4: 4940.
  46. Bai ZG, Yu DP, Wang JJ, Zou YH, Qian W, Fu JS, et al. Synthesis and photoluminescence properties of semiconductor nanowires. *Mater Sci Eng B-Solid State Mater Adv Technol*. 2000; 72: 117-120.
  47. Charrier J, Najar A, Pirasteh P. Study of optical absorbance in porous silicon nanowires for photovoltaic applications. *Appl Surf Sci*. 2013; 283: 828-832.
  48. Lin LH, Sun XZ, Tao R, Li ZC, Feng JY, Zhang ZJ. Photoluminescence origins of the porous silicon nanowire arrays. *J Appl Phys*. 2011; 110: 073109.
  49. Lin L, Guo S, Sun X, Feng J, Wang Y. Synthesis and Photoluminescence Properties of Porous Silicon Nanowire Arrays. *Nanoscale Res Lett*. 2010; 5: 1822-1828.
  50. Jin C, Kim H, Hong C, Park S, Lee C. Influence of SnO<sub>2</sub> coating and annealing on the luminescence properties of porous silicon nanowires. *Mater Lett*. 2011; 65: 3275-3277.
  51. Lin LH, Li ZC, Feng JY, Zhang ZJ. Direct radiative recombination in the Se-terminated nanoscale Si porous structure. *Appl Surf Sci*. 2012; 258: 6977-6981.
  52. Hu L, Chen G. Analysis of optical absorption in silicon nanowire arrays for photovoltaic applications. *Nano Lett*. 2007; 7: 3249-3252.
  53. To WK, Fu J, Yang X, Roy VA, Huang Z. Porosification-reduced optical trapping of silicon nanostructures. *Nanoscale*. 2012; 4: 5835-5839.
  54. Huang Z, Hawkey MM, Brett MJ. Enhancement in broadband and quasi-omnidirectional antireflection of nanopillar arrays by ion milling. *Nanotechnology*. 2012; 23: 275703.
  55. de Smet LCPM, Ullien D, Mescher M, Sudhölter EJR. Organic Surface Modification of Silicon Nanowire-Based Sensor Devices. In: Hashim A (ed). *Nanowires - Implementations and Applications*. InTech, 2011.
  56. Weisse JM, Kim DR, Lee CH, Zheng X. Vertical transfer of uniform silicon nanowire arrays via crack formation. *Nano Lett*. 2011; 11: 1300-1305.
  57. Weisse JM, Lee CH, Kim DR, Cai L, Rao PM, Zheng X. Electroassisted transfer of vertical silicon wire arrays using a sacrificial porous silicon layer. *Nano Lett*. 2013; 13: 4362-4368.

#### Cite this article

Huang Z, Liu J (2015) Silicon Nanowires with Mesopores: Fabrication and Optical Properties. *JSM Nanotechnol Nanomed* 3(1): 1035.